J Adv Ceram

Research Article

Realizing negative thermal expansion over an extended temperature range in $PbTiO_3$-based perovskites

Zhao Pan[1,✉], Fengyi Zhou[2], Mengqi Ye[1], Duo Wang[2], Qiumin Liu[3], Takumi Nishikubo[3,4], Xubin Ye[1], Xiao Wang[1], Jin Liu[1], Nianpeng Lu[1], Shogo Kawaguchi[5], Masaki Azuma[3,4], Youwen Long[1,6,✉]

Cite this article: Pan Z, Zhou F, Ye M, et al. *J Adv Ceram* 2025, **14**: 9221096. https://doi.org/10.26599/JAC.2025.9221096

ABSTRACT: Negative thermal expansion (NTE) is fascinating, as it involves a material's volume contraction rather than expansion upon heating. Although NTE lattices typically have highly flexible frameworks, the magnitude of NTE is often very small, and they frequently exhibit a narrow temperature range for controllable NTEs. It remains a great challenge to achieve large NTE while maintaining a wide temperature operation range from the currently available materials. Herein, we present a novel $PbTiO_3$ (PT)-based perovskite system, $(1-x)PbTiO_3$–$xBiYbO_3$, synthesized via a distinctive high-pressure and high-temperature technique. Compared with pristine $PbTiO_3$ (c/a = 1.064), the system exhibited unusual enhanced tetragonalities. Consequently, NTE over an extended temperature range has been realized in $0.95PbTiO_3$–$0.05BiYbO_3$ ($\bar{\alpha}_V = -2.18\times10^{-5}$ K^{-1}, 300–820 K) and $0.90PbTiO_3$–$0.10BiYbO_3$ ($\bar{\alpha}_V = -1.85\times10^{-5}$ K^{-1}, 300–850 K) compared with that of pristine $PbTiO_3$ ($\bar{\alpha}_V = -1.99\times10^{-5}$ K^{-1}, 300–763 K). Our experimental and theoretical studies indicate that the improved tetragonality and expanded NTE temperature range result from larger ionic displacements and an enhanced asymmetric charge distribution, both of which are induced by $BiYbO_3$ substitution. The present study presents a new example of an NTE across a broad temperature range, highlighting its potential as an effective thermal expansion compensator.

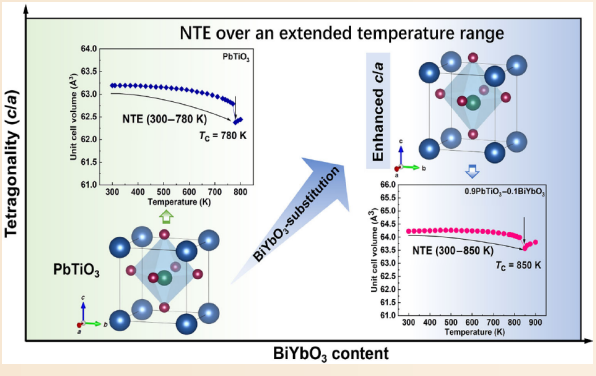

KEYWORDS: negative thermal expansion (NTE); $PbTiO_3$ (PT)-based perovskites; Curie temperature (T_C); high-pressure and high-temperature method; density functional calculations

1 Introduction

Materials commonly expand upon heating and contract upon cooling as a result of normal positive thermal expansion (PTE). Note that a linear distortion as small as 1 mm can significantly compromise the performance of high-precision instruments [1–4]. Additionally, a mismatched coefficient of thermal expansion (CTE) between components in devices composed of multiple materials can also result in severe damage, such as interface shedding or even fracture. Hence, the control of the thermal expansion of materials is a crucial issue in advanced electronic equipment. However, controlling thermal expansion is a common problem that is difficult to solve. In recent decades, the discovery of negative thermal expansion (NTE) materials, in which the volume decreases upon heating, holds promise for use as thermal expansion compensators in PTE materials or even for realizing zero thermal expansion (ZTE) composites [5].

To date, several types of materials with potential as NTE materials have been explored and identified. In addition to the well-known framework NTE materials of the ZrW_2O_8 family [6], NTE effects have also been observed in Invar alloys [7–9], $Ag_3[Co(CN)_6]$ cyanides [10–12], ScF_3 fluorides [13–15], Mn_3AN (A = Cu, Ge, etc.) magnetic nitrides [16–18], layered ruthenate $Ca_2RuO_{3.74}$ [19–21], and $PbTiO_3$ (PT)-based ferroelectrics [22–24]. However, considering the small magnitude and relatively narrow temperature window of NTE, very few NTE materials can be used as high-performance thermal expansion inhibitors. For example, traditional NTE materials with flexible framework structures usually exhibit NTE over a broad temperature range up to 1000 K, but the related average volumetric CTE can hardly exceed -10×10^{-6} K^{-1} [6]. Therefore, to achieve high-performance ZTE composites, an abundance of NTE additions is usually needed. Note that many phase-transition-type NTE materials have strong NTEs during phase transitions [25–27]. However, NTE in

[1]Beijing National Laboratory for Condensed Matter Physics, Institute of Physics, Chinese Academy of Sciences, Beijing 100190, China. [2]Faculty of Applied Sciences, Macao Polytechnic University, Macao 999078, China. [3]Laboratory for Materials and Structures, Tokyo Institute of Technology, Yokohama 226-8503, Japan. [4]Kanagawa Institute of Industrial Science and Technology (KISTEC), Kanagawa 243-0435, Japan. [5]Research and Utilization Division, Japan Synchrotron Radiation Research Institute (JASRI), Hyōgo 679-5198, Japan. [6]Songshan Lake Materials Laboratory, Dongguan 523808, China.

✉ Corresponding authors. E-mail: Z. Pan, zhaopan@iphy.ac.cn; Y. Long, ywlong@iphy.ac.cn

Received: January 15, 2025; Revised: May 16, 2025; Accepted: May 19, 2025

those materials usually occurs only in a very limited temperature range (< 200 K), which also hinders their application. Therefore, achieving large NTE over a wide temperature range remains a challenge.

It has been suggested that perovskite-type (ABO_3) ferroelectric PT is one of the most promising compounds for large NTE applications. In addition to piezoelectricity and ferroelectricity [28], PT also exhibits an unusual NTE from room temperature (RT) to its Curie temperature (T_C = 763 K), with a pronounced average volumetric CTE of $\alpha_V = 1.99\times10^{-5}\,K^{-1}$ [29]. As the volume shrinkage of PT occurs primarily along the polar *c* axis of the tetragonal phase, an increase in tetragonality (*c*/*a*) could lead to an increase in the NTE. Indeed, enhanced NTEs were obtained in PT-based ferroelectrics with improved tetragonality [23,24]. The flexible structure of PT allows for the enhancement of the NTE by modulating its *c*/*a*. Inspired by the proposed relationship between the tolerance factor and *c*/*a* in PT-$BiMeO_3$ (Me represents a mixture of cations with an average valence of +3) systems [30], herein, we designed and prepared a new PT-based perovskite system of (1–*x*)PT–*x*$BiYbO_3$, which has an enhanced *c*/*a* in comparison with that of pristine PT (*c*/*a* = 1.064). As expected, a large NTE over an extended temperature range was successfully achieved. A systematic study was conducted on the crystal structure, thermal expansion properties, and related mechanisms.

2 Materials and methods

Materials preparation. A cubic anvil-type high-pressure apparatus was used to prepare samples of the (1–*x*)$PbTiO_3$–*x*$BiYbO_3$ (*x* = 0, 0.05, and 0.10, hereinafter referred to as (1–*x*)PT–*x*BY) compounds. The raw materials of high-purity PbO (99.999%, Aladdin, China), TiO_2 (99.99%, Aladdin, China), Bi_2O_3 (99.99%, Innochem, China), and Yb_2O_3 (99.9%, Macklin, China) were thoroughly mixed according to stoichiometry. The mixtures were then sealed in a gold capsule and reacted at 6 GPa and 1373 K for 30 min. To remove the mechanical strain introduced during high-pressure synthesis, the obtained samples were carefully ground and annealed at 400 °C for 1 h before cooling to room temperature.

Characterizations. An X-ray diffractometer (XRD; G670, Huber, Germany) was used to collect X-ray diffraction (XRD) patterns for phase identification. High-temperature synchrotron X-ray powder diffraction (SXRD) experiments were performed on the BL02B2 beamline of SPring-8 with a wavelength of 0.42 Å. Using FullProf software (version: June-2015), the detailed crystal structure was refined on the basis of the full-profile Rietveld method. The selected area electron diffraction (SAED) experiments were performed on a transmission electron microscope (TEM; ARM200F, JEOL, Japan) (with a field-emission gun (FEG) and a JEM-2100 Plus, JEOL, Japan) operating at 200 kV. A spectrometer (MonoVista CRS+ 500, Spectroscopy & Imaging GmbH, Germany) was used to collect Raman scattering spectra.

First-principles calculations. The structural models were constructed on the basis of experimental crystallographic measurements. During geometry optimization, only the internal atomic positions were allowed to relax, while the structure volume and shape were constrained to maintain their experimental values. To properly account for the 5% doping effect (i.e., the 0.95PT–0.05BY composition), a 2 × 5 × 2 supercell comprising 100 atoms was constructed, with the structural model provided in the Supporting Information. All the simulations were executed via the Vienna *ab initio* simulation package (VASP, version 6.4.1), a first-principles density functional theory (DFT) code that employs a plane-wave basis set [31] and the projector-augmented (PAW) method [32]. The generalized gradient approximation (GGA) with the Perdew–Burke–Ernzerhof (PBE) functional [33] was employed to describe the electron exchange-correlation interactions [34], which has been validated, with a supporting justification provided in the Supporting Information. The kinetic plane wave energy cutoff was set to 520 eV to ensure the convergence of the calculations. Geometry optimization and all electronic structures, as well as electron localization functions (ELFs) [35,36] were conducted with convergence criteria of 0.01 eV/Å for the forces and 1×10^{-6} eV for the total energy, using Brillouin zone meshes of 5 × 2 × 5 and 7 × 3 × 7 *k*-points, respectively. The crystal orbital Hamilton population (COHP) [37–39] was used to analyze the bonding state, as it is implemented in the Local Orbital Basis Suite Toward Electronic-Structure Reconstruction (LOBSTER) program [40].

3 Results and discussion

Crystal structure. The XRD patterns of (1–*x*)PT–*x*BY (*x* = 0.0–0.10) at room temperature are depicted in Fig. 1(a). The samples are of high quality with negligible impurities, and all investigated samples have tetragonal symmetry. The precise structural parameters were refined via the SXRD data and are listed in the Electronic Supplementary Material (ESM) (Figs. S1–S3 and Tables S1 and S2 in the ESM). According to the Rietveld refinement results, the *c* axis clearly tends to increase with the substitution of $BiYbO_3$, whereas the *a* axis slightly increases as a function of the $BiYbO_3$ content. Consequently, the *c*/*a* ratio increases from 1.064 for pristine PT to 1.066 and 1.069 for

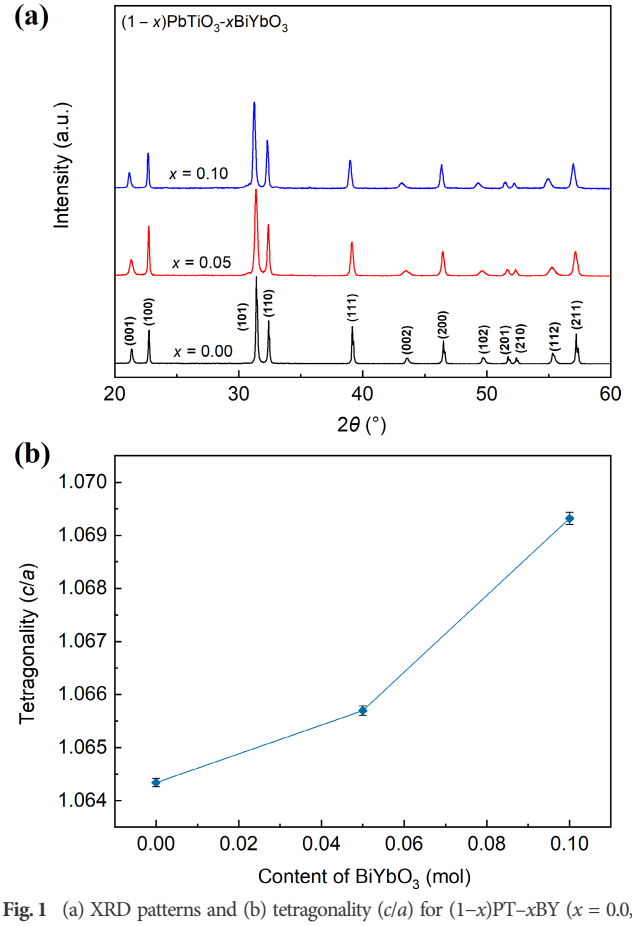

Fig. 1 (a) XRD patterns and (b) tetragonality (*c*/*a*) for (1–*x*)PT–*x*BY (*x* = 0.0, 0.05, and 0.10) compounds at room temperature.

0.95PT–0.05BY and 0.90PT–0.10BY, respectively (Fig. 1(b)), indicating enhanced tetragonality by the substitution of $BiYbO_3$. The SAED patterns of the 0.95PT–0.05BY and 0.90PT–0.10BY compounds at room temperature further confirmed their tetragonal character (Fig. S4 in the ESM). The large lattice distortions can be attributed to the strong Pb/Bi–O and Ti/Yb–O coupling interactions between the Pb/Bi and Ti/Yb cations, resulting in large spontaneous polarization (P_S) displacements. In ABO_3 perovskite-type ferroelectrics, P_S originates from the displacement of the A- and B-site cations away from the centroid of the oxygen polyhedra (inset of Fig. S5(a) in the ESM). On the basis of the Rietveld refinement of the SXRD data, P_S displacements for Pb/Bi on the A-site (δz_A) and Ti/Yb on the B-site (δz_B) can be estimated by considering a purely ionic crystal and neglecting the electronic polarization via Eq. (1) [41]:

$$P_S = Z\sum_i \frac{\delta z_i q_i}{V} \quad (1)$$

where δz_i indicates that the cation shifts along the ferroelectric axis of the ith ion with the electric charge (q_i), V represents the unit cell volume, and Z equals 1. Both δz_A and δz_B tend to increase with the addition of $BiYbO_3$ (Fig. S5(a) in the ESM). Accordingly, P_S of 0.95PT–0.05BY and 0.90PT–0.10BY increases from 44 μC/cm² for pristine PT to 57 and 59 μC/cm² for 0.95PT–0.05BY and 0.90PT–0.10BY, respectively (Fig. S5(b) in the ESM), which agrees well with the enhanced tetragonality.

Lattice dynamics. It is suggested that ferroelectric phase transitions are associated with vibrational soft modes on the basis of lattice dynamical theory [42]. On the basis of lattice dynamics, the frequency of the A_1(1TO) soft mode is proportional to P_S because it represents the displacement of the TiO_6 octahedron relative to Pb. The A_1(1TO) soft mode is almost linearly related to the displacement of A-site atoms in PT-based compounds, both with normally reduced and abnormally enhanced c/a values [43]. For example, $Pb_{1-x}Cd_xTiO_3$ has been observed to have an enhanced c/a along with hardened A_1(1TO) [44], whereas a decrease in c/a and a softened A_1(1TO) mode have been observed in $Pb_{1-x}Sr_xTiO_3$ [45]. In addition to the A_1(1TO) soft mode, the A_1(2TO) soft mode is sensitive to B-site atom displacements since it indicates the displacement of B-site atoms relative to the oxygen and A-site atoms [30]. Figure 2 shows the Raman spectra of the (1–x)PT–xBY (x = 0.0, 0.05, and 0.10) solid solutions and their soft modes. Interestingly, the Raman active modes of A_1(1TO) and A_1(2TO) shift toward higher frequencies with increasing $BiYbO_3$ content, which is consistent with the enhanced P_S displacements at both the A-site and B-site from the Rietveld refinement results.

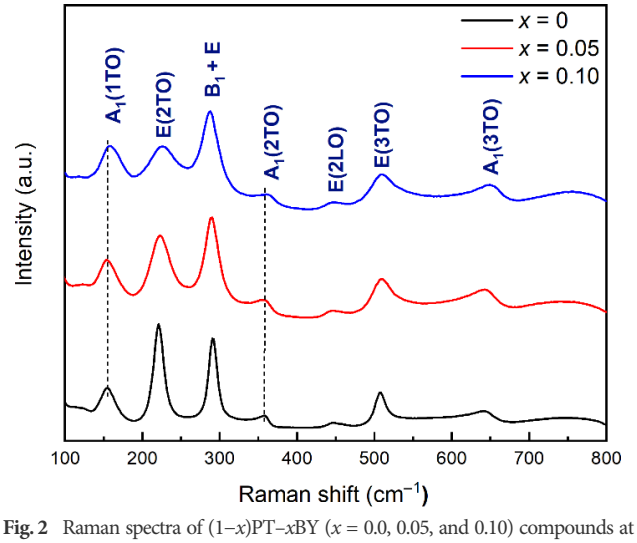

Fig. 2 Raman spectra of (1–x)PT–xBY (x = 0.0, 0.05, and 0.10) compounds at room temperature.

Thermal expansion properties. In ferroelectrics based on PT, the increased c/a and large P_S could be associated with a large ferroelectric volume effect or a large NTE [24]. It is proposed that a large c/a of PT-based ferroelectrics indicates large lattice distortion, which could lead to significant volume shrinkage when the lattice energy is released upon heating. Consequently, enhanced NTE was observed, such as in $(Pb_{0.94}Cd_{0.06})TiO_3$ (c/a = 1.069, $\bar{\alpha}_V$ = −2.40×10⁻⁵ K⁻¹) [44], 0.4PT–0.6$BiFeO_3$ (c/a = 1.165, $\bar{\alpha}_V$ = −3.92×10⁻⁵ K⁻¹) [23], and the recently reported $Pb(Ti_{0.7}V_{0.3})O_3$ (c/a = 1.11, ΔV = −3.7%, where ΔV means volume changes) [46], which exhibited abnormally increased c/a and NTE in comparison with those of pristine PT. To study the thermal expansion properties of (1–x)PT–xBY (x = 0.05 and 0.10) solid solutions, temperature-dependent SXRD experiments were performed. The temperature dependence of the lattice parameters of the (1–x)PT–xBY (x = 0.05 and 0.10) compounds was determined by Rietveld refinement of the SXRD data (Figs. 3(a) and 3(b)). The c axis decreases rapidly with increasing temperature, whereas the $a(b)$ axis slightly increases with increasing temperature for both the 0.95PT–0.05BY and 0.90PT–0.10BY compounds. Consequently, for the 0.95PT–0.05BY compound, in the temperature range of RT to 700 K, the unit cell volume shows little dependence on the temperature, with the average CTE of −3.79×10⁻⁶ K⁻¹. However, a very strong NTE occurs near the T_C. The average volumetric CTE over the whole temperature range of 300–820 K was $\bar{\alpha}_V$ = −2.18×10⁻⁵ K⁻¹ (Fig. 3(c)), which is even slightly stronger than that of pristine PT ($\bar{\alpha}_V$ = −1.99×10⁻⁵ K⁻¹, 300–763 K). A similar phenomenon was also observed for the 0.90PT–0.10BY compound. In the temperature range of RT to 700 K, the low CTE of −1.31×10⁻⁶ K⁻¹ was observed, whereas a sharp decrease in the unit cell volume occurred with increasing temperature. The overall volumetric CTE of 0.90PT–0.10BY is $\bar{\alpha}_V$ = −1.85×10⁻⁵ K⁻¹ in the temperature range of RT to 850 K. Note that even though the magnitude of NTE for the 0.90PT–0.10BY compound decreased, the NTE temperature range was extended from RT to T_C as high as 850 K (Fig. 3(d)). Here, the increased T_C also coincides with the increased tetragonality and P_S.

Mechanism of NTE in (1–x)PT–xBY compounds. Experimental and theoretical studies have shown that ferroelectric behavior has a significant influence on the NTEs of PT-based ferroelectrics [3]. A new physical concept of spontaneous volume ferroelectrostriction (SVFS, ω_S) has recently been proposed to quantify how ferroelectricity affects abnormal volume changes in ferroelectric phases of PT-based ferroelectrics [47]. Equation (2) is a definition of SVFS:

$$\omega_S = \frac{V_{exp} - V_{nm}}{V_{nm}} \times 100\% \quad (2)$$

In Eq. (2), V_{exp} represents the experimental cell volume, V_{nm} represents the nominal unit cell volume, and V_{nm} can be estimated via extrapolation from the paraelectric to the ferroelectric phase. A high ω_S value signifies a robust ferroelectrovolume effect and enhanced NTE, whereas a low value indicates a weak NTE. Here, the ω_S values are 3.30% and 2.76% for 0.95PT–0.05BY and 0.90PT–0.10BY (Fig. 3), respectively, which are consistent with the enhanced and weakened NTE observed in 0.95PT–0.05BY and 0.90PT–0.10BY, respectively, compared with the pristine PT with ω_S of 3.1% [3].

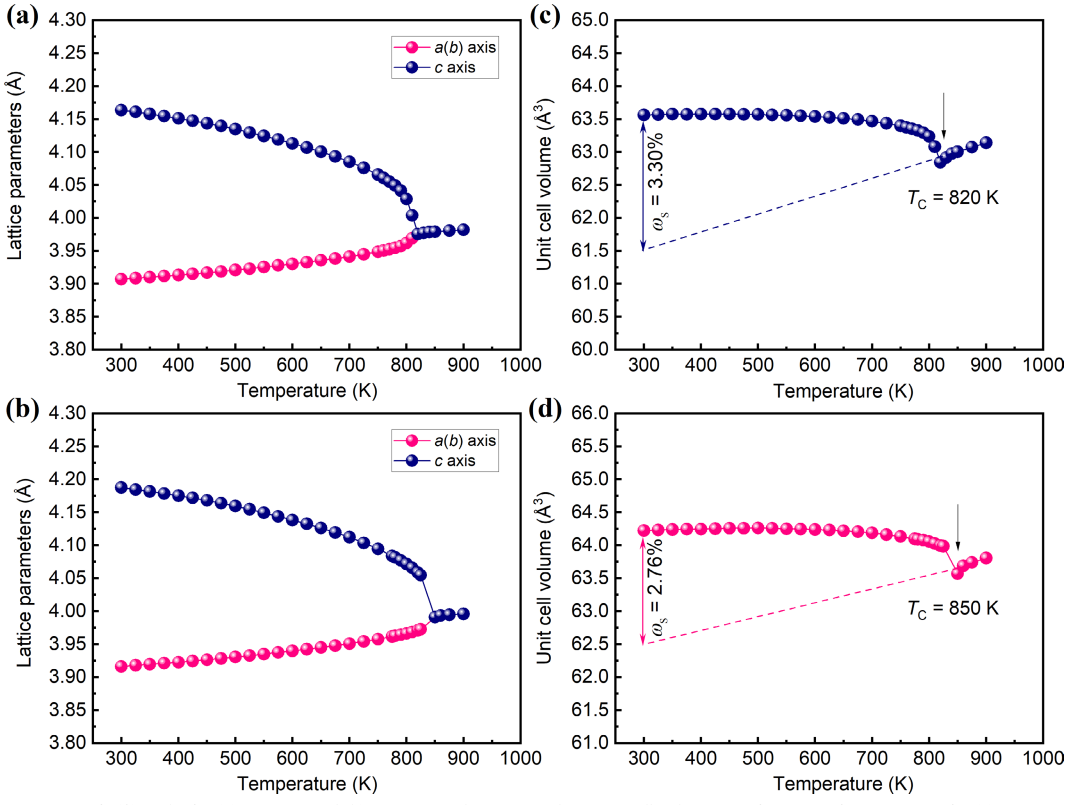

Fig. 3 Lattice parameters of $a(b)$ and c for (a) $x = 0.05$ and (b) $x = 0.10$ and corresponding unit cell volume as a function of temperature for (c) $x = 0.05$ and (d) $x = 0.10$ of $(1-x)$PT–xBY compounds. An illustration of ω_S is also provided.

Theoretical calculations. It has been proposed that NTE in PT-based ferroelectrics depends critically on hybridization between the cations and anions [48,49]. To intuitively study the effect of $BiYbO_3$ substitution on hybridization, we performed *ab initio* simulations of $(1-x)$PT–xBY (x = 0 and 0.05) to further understand the enhanced electric polarization and NTE in 0.95PT–0.05BY (Figs. S6–S9 in the ESM). As both off-center ionic displacement and electronic redistribution contribute to electric polarization, we first determined the ground-state crystal structure by performing internal atomistic optimization. The representative atomic positions are shown in Fig. 4. Compared with that of pristine PT, the most obvious atomic displacement induced by $BiYbO_3$ substitution occurred at the B-site positions along the electric polarization direction ($-c$) as shown in Fig. 4. The average magnitude of the displacement increased from 0.03 Å in the pristine PT to 0.20 and 0.17 Å, respectively, for Ti and Yb in 0.95PT–0.05BY, indicating a substantial ionic contribution to the system's ferroelectricity. In contrast, A-site atoms exhibit displacements of 0.15 and 0.04 Å for Bi and Pb, respectively, compared with 0.007 Å in the original PT structure, with only the Bi displacement being comparable to the values obtained at the B-site atoms. These observations indicate that the $BiYbO_3$ substitution enhanced the interaction on the shorter A/B–O bond, resulting in increased electric polarization, tetragonality, and NTE.

The electronic contribution, on the other hand, can be understood by exploring the asymmetric charge redistribution introduced by the $BiYbO_3$ substitution. The ELF is one of the most effective tools for examining these features. For the B-site atoms, the electronic localization was examined by comparing the characteristics around the Ti and Yb atoms. Compared with the negligible likelihood of finding electrons between Ti and the neighboring O atoms in Fig. 4(a) (shown in blue), Yb substitution not only introduces more electrons into the system but also, more importantly, establishes a significant asymmetric redistribution of charge along the c-axis, as illustrated in Fig. 4(b) (shown in cyan). This additional electronic contribution provides the system with extra degrees of freedom in elevating ferroelectric polarization. For the A-site atoms, Bi substitution introduces a minor expansion of

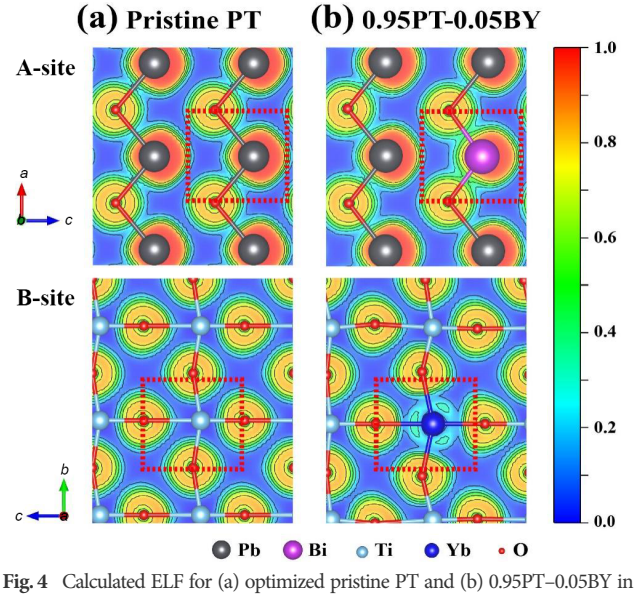

Fig. 4 Calculated ELF for (a) optimized pristine PT and (b) 0.95PT–0.05BY in *ac* plane and *bc* plane. ELF values are color-mapped from blue to green to red with a scale from 0 to 1, as indicated by scale bar in right panel. Regions with ELF = 0.5 correspond to a homogeneous electron gas; any increase in ELF value denotes a strengthening of covalent interactions. A-site atoms (Pb and Bi), B-site atoms (Ti and Yb), and O atoms are represented by dark gray, purple, cyan, blue, and red spheres, respectively. The red dashed rectangles denote ELF before and after A-site and B-site substitution.

the electron localization region (green), indicating an increased occupancy of shared electrons between Bi and O.

To provide a more quantitative explanation of the bonding nature in 0.95PT–0.05BY, we performed COHP bonding analysis. The –COHP data are shown in Fig. 5. In general, the bonding states of the four A/B bonds are predominantly located below the Fermi level, with the corresponding antibonding states elevated by nearly 4 eV. An exception is observed for the Yb–O bond, where the bond strength is reduced due to the presence of antibonding states at two separate energy levels, approximately −2 and −15 eV. These bond strengths are well reflected in the integrated –COHP data, as listed in Table 1. Moreover, the bond strengths among the three A/B–O bonds clearly correlate with the bond type: the A/B–O_3 bond is the strongest, A/B–O_2 has intermediate strength, and A/B–O_1 is relatively weak. This trend holds regardless of whether the absolute bond strength is significantly enhanced, as in the Bisubstituted case, or reduced, as in the Yb-substituted case. These observations strongly support our argument that there exists a variation in the bond strength around each cation site, resulting in an overall asymmetric charge distribution.

This enhancement of the bond between the substituted atom and the ligand O in a specific direction can be further validated by the electronic characteristics exhibited in their density of states (DOS). The overall DOS distribution is determined by the energy levels of electrons on the bonded atoms, and the relative intensity variation reflects changes in electron occupancy, which is consistent with the bond strength enhancement discussed in the COHP results. As illustrated in Figs. 6(a) and 6(b), each A-site (or B-site) atom is surrounded by twelve (or six) nearest neighboring O atoms, forming an AO_{12} (or BO_6) polyhedral local environment. Owing to the cation displacement that mainly occurred along the −*c* direction, the nearest A–O and B–O bonds can be classified into three categories, l_1, l_2, and l_3, on the basis of their degenerate bond lengths (Table S3 in the ESM), and thus exhibit three types of electronic DOSs (Fig. S10 in the ESM). Among the three bonds, l_1 and l_3 feature similar geometric environments, with the only difference being a change in length along the *c* direction. As shown in Figs. 6(c) and 6(d), the corresponding oxygen DOSs therefore exhibit similar energy-dependent spectral functions (upper and lower panels). In contrast, the oxygen DOSs corresponding to the l_2 bond exhibit a modified and reshaped intensity distribution (middle panel). Taking PbO_{12} as an example, both the l_1 and l_3 oxygen DOSs exhibit an overall similar shape, with two peaks occurring at energy levels of −4 and −1 eV, whereas the l_2 DOS exhibits an intensified peak located near −2 eV. On the other hand, the introduction of cation substitution significantly changes the DOS shape. As the A-site atom changes from Pb to Bi, a characteristic DOS peak appears at −5 eV, thereby promoting DOS overlap with nearby oxygen atoms. However, this A-site substitution has only a minor effect on the interaction strength. In contrast, as shown in Fig. 6(d), when the B-site Ti atom is substituted by a Yb atom, the DOSs on the O atoms become more localized at energy states close to the Fermi level and, more critically, significantly intensify the electronic state distribution across all the oxygen atoms. In addition, and most importantly, the previously nearly identical O_1 and O_3 DOSs are now differentiated: A much more significant O_3 DOS is observed, with its peak intensity almost twice that of the other oxygen atoms. This feature indicates a Yb-induced nontrivial electronic state, such as a flat band or a von Hove singularity (VHS) around the Fermi level, which has been proven to have a close relationship with the enhanced NTE identified in previous studies [50,51]. A von Hove singularity arises from a critical point (either an extremum or a saddle point) in the electronic band structure and manifests as a divergence in the DOS in a crystalline solid. Although such a feature can be suggested or indirectly observed in the calculated electronic DOS [52], more direct evidence would come from a well-resolved

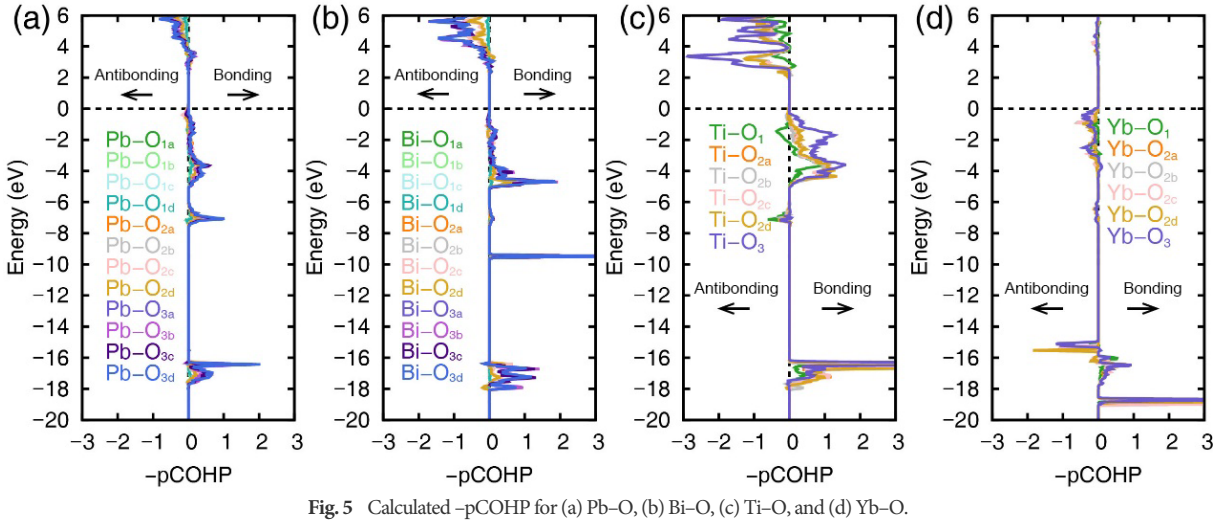

Fig. 5 Calculated –pCOHP for (a) Pb–O, (b) Bi–O, (c) Ti–O, and (d) Yb–O.

Table 1 Calculated average integral –COHP for A/B–O bond (A = Pb/Bi, B = Ti/Yb)

		Integrated –COHP		
		A/B–O_1	A/B–O_2	A/B–O_3
A-site	Pb	0.200	0.790	1.519
	Bi	0.105	0.714	2.341
B-site	Ti	1.813	4.093	6.504
	Yb	0.279	0.327	0.371

electronic band structure or, more conveniently, from constant energy contours in the first Brillouin zone at the corresponding energy level.

The calculated electronic band structure is shown in Fig. 7(a), alongside a zoomed-in view of the DOS. At the Fermi level, von Hove singularity features are observed at the Γ and X points. At the energy level corresponding to the O_3 peak (−0.423 eV), the bands are more complex, suggesting the presence of potential critical features at the Γ, D, A_2, and H_1 points. These features manifest more clearly as a two-dimensional pocket in the energy surface at the corresponding energy level, indicative of von Hove filling, as illustrated in Figs. 7(b) and 7(c).

Overall, by performing a self-consistent theoretical study of the electronic structures of 0.95PT–0.05BY, we validated the crucial role of both the ionic and electronic contributions resulting from $BiYbO_3$ substitution. More importantly, further analysis indicates

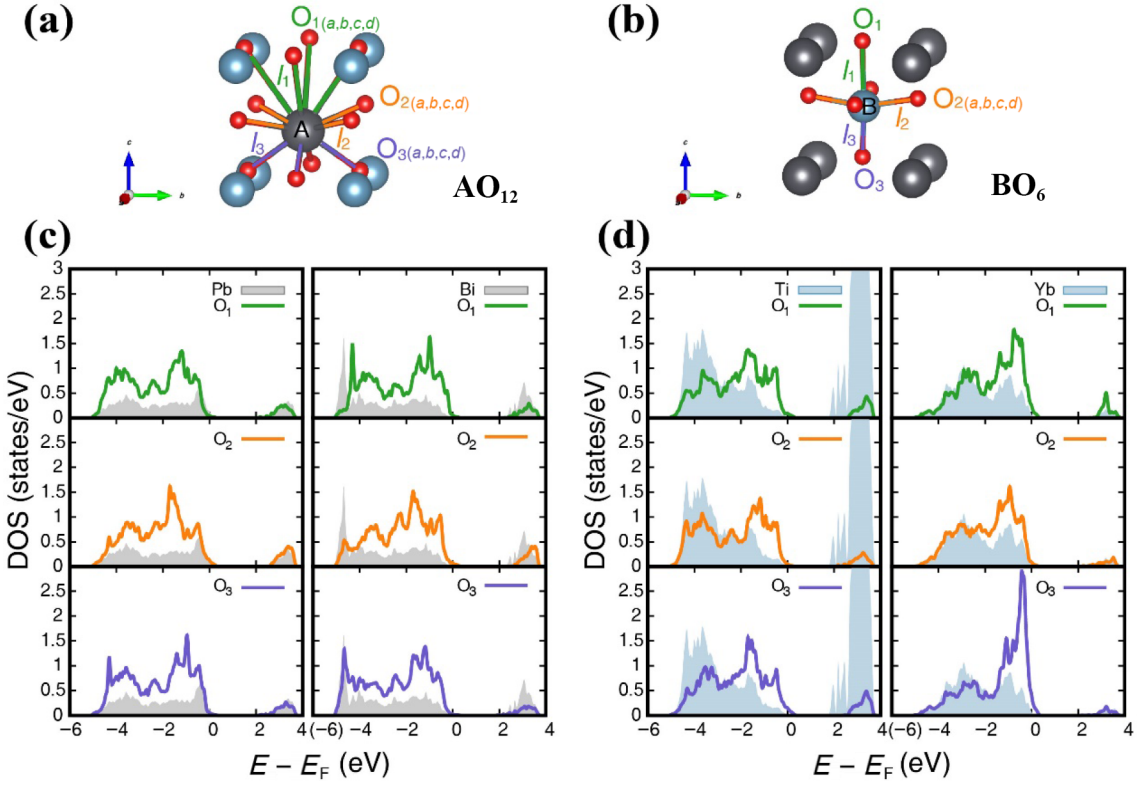

Fig. 6 Representative structures of local (a) AO_{12} and (b) BO_6 environments at 0.95PT–0.05BY. A-site, B-site, and O atoms are depicted as dark gray, cyan, and red spheres, respectively. Calculated electronic DOS in (c) AO_{12} and (d) BO_6. Green, orange, and purple lines in structure and DOS plots indicate long (l_1), medium (l_2), and short (l_3) bonds around each cation atom and corresponding DOS.

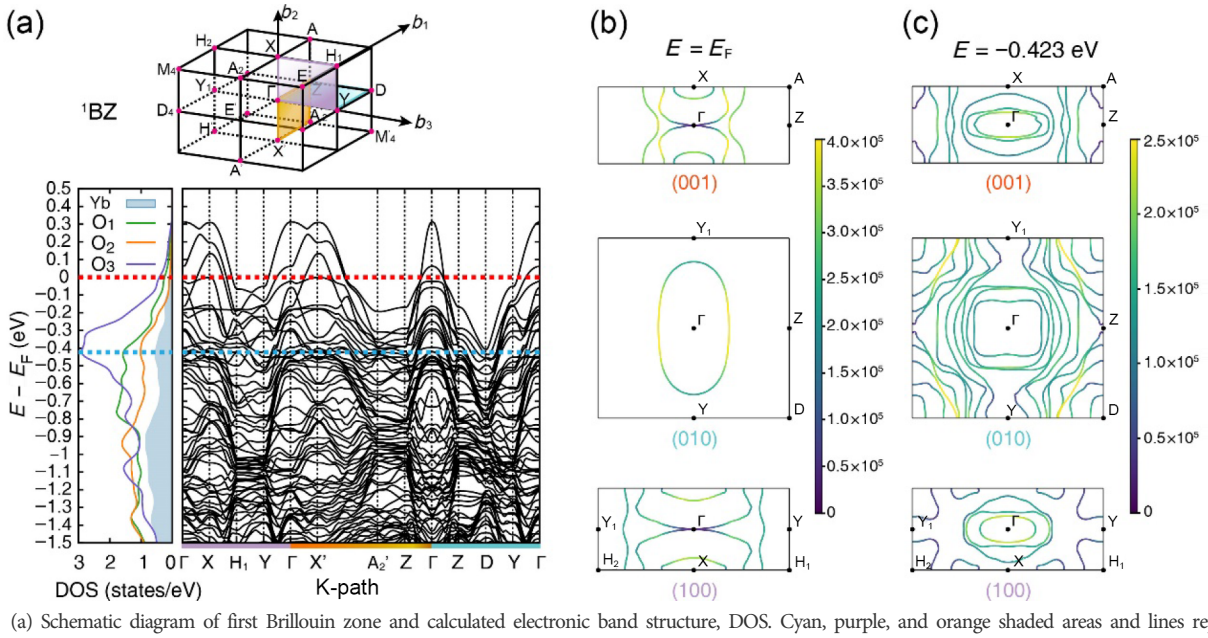

Fig. 7 (a) Schematic diagram of first Brillouin zone and calculated electronic band structure, DOS. Cyan, purple, and orange shaded areas and lines represent characteristic high-symmetry paths. Red and cyan horizontal dashed lines represent Fermi level and O_3 peak energy (−0.423 eV), respectively. Constant energy contours in first Brillouin zone at (b) Fermi level and (c) O_3 DOS peak. Results for (001), (010), and (100) planes are shown from top to bottom.

that the Yb-induced charge redistribution might cause a nontrivial electronic state, specifically a von Hove singularity around the Fermi surface, which, in turn, is expected to be the reason for the experimentally observed increase in negative thermal expansion.

4 Conclusions

In conclusion, we designed and prepared a new PT-based ferroelectric of (1–*x*)PT–*x*BY with enhanced tetragonality compared with that of pristine PT by using a high-pressure and high-temperature method. As a result, a strong NTE over an extended temperature range was successfully achieved, which contrasts with that of pristine PT. On the basis of our experimental and theoretical studies, we attributed the large NTE to the enhanced P_S induced by the substitution of $BiYbO_3$. This work offers a new example of an NTE over a wide temperature range, which shows potential as a high-performance thermal expansion compensator.

Acknowledgements

We thank Prof. Xi Shen at the Institute of Physics, Chinese Academy of Sciences, for the TEM experiments. This work was supported by the National Key R&D Program of China (No. 2021YFA1400300), the National Natural Science Foundation of China (Nos. 22271309, 12304268, 12425403, and 12261131499), the Beijing Natural Science Foundation (No. F251005), and the Chinese Academy of Sciences (No. XDB33000000). Duo Wang acknowledges financial support from the Science and Technology Development Fund from Macau SAR (No. 0062/2023/ITP2) and the Macao Polytechnic University (No. RP/FCA-03/2023). The synchrotron X-ray powder diffraction experiments were performed at SPring-8 with the approval of the Japan Synchrotron Radiation Research Institute (Nos. 2024A1506 and 2024A1695).

Author contributions

Zhao Pan: writing—original draft, review, and editing, conceptualization, data curation, formal analysis, funding acquisition, investigation, and project administration; Fengyi Zhou: writing—original draft, review, and editing, formal analysis, and software; Mengqi Ye: data curation and investigation; Duo Wang: writing—original draft, review, and editing, formal analysis, funding acquisition, and software; Qiumin Liu: data curation; Takumi Nishikubo: data curation; Xubin Ye: data curation; Xiao Wang: data curation; Jin Liu: data curation; Nianpeng Lu: data curation; Shogo Kawaguchi: data curation; Masaki Azuma: data curation and resources; Youwen Long: writing—review & editing, funding acquisition, and resources.

Availability of data and materials

The data that support the findings of this study are available from the corresponding author upon reasonable request.

Competing interests

The authors have no competing interests to declare that are relevant to the content of this article.

Electronic Supplementary Material

Supplementary material is available in the online version of this article at https://doi.org/10.26599/JAC.2025.9221096.

References

[1] Takenaka K. Progress of research in negative thermal expansion materials: Paradigm shift in the control of thermal expansion. *Front Chem* 2018, **6**: 267.
[2] Attfield JP. Mechanisms and materials for NTE. *Front Chem* 2018, **6**: 371.
[3] Chen J, Hu L, Deng JX, *et al.* Negative thermal expansion in functional materials: Controllable thermal expansion by chemical modifications. *Chem Soc Rev* 2015, **44**: 3522–3567.
[4] Luo BC, Feng W, Dai SW, *et al.* Stabilizing oxygen vacancies and promoting electrostrain in lead-free potassium niobate-based piezoelectrics over wide temperature ranges. *J Adv Ceram* 2024, **13**: 1965–1973.
[5] Takenaka K. Negative thermal expansion materials: Technological key for control of thermal expansion. *Sci Technol Adv Mat* 2012, **13**: 013001.
[6] Mary TA, Evans JSO, Vogt T, *et al.* Negative thermal expansion from 0.3 to 1050 kelvin in ZrW_2O_8. *Science* 1996, **272**: 90–92.
[7] van Schilfgaarde M, Abrikosov IA, Johansson B. Origin of the Invar effect in iron-nickel alloys. *Nature* 1999, **400**: 46–49.
[8] Song YZ, Chen J, Liu XZ, *et al.* Zero thermal expansion in magnetic and metallic $Tb(Co,Fe)_2$ intermetallic compounds. *J Am Chem Soc* 2018, **140**: 602–605.
[9] Lin K, Li WJ, Yu CY, *et al.* High performance and low thermal expansion in Er–Fe–V–Mo dual-phase alloys. *Acta Mater* 2020, **198**: 271–280.
[10] Goodwin AL, Calleja M, Conterio MJ, *et al.* Colossal positive and negative thermal expansion in the framework material $Ag_3[Co(CN)_6]$. *Science* 2008, **319**: 794–797.
[11] Gao Q, Wang J, Sanson A, *et al.* Discovering large isotropic negative thermal expansion in framework compound $AgB(CN)_4$ via the concept of average atomic volume. *J Am Chem Soc* 2020, **142**: 6935–6939.
[12] Gao Q, Jiao Y, Sun Q, *et al.* Giant negative thermal expansion in ultralight $NaB(CN)_4$. *Angew Chem Int Edit* 2024, **63**: e202401302.
[13] Greve BK, Martin KL, Lee PL, *et al.* Pronounced negative thermal expansion from a simple structure: Cubic ScF_3. *J Am Chem Soc* 2010, **132**: 15496–15498.
[14] Hu L, Chen J, Fan LL, *et al.* Zero thermal expansion and ferromagnetism in cubic $Sc_{1-x}M_xF_3$ (M = Ga, Fe) over a wide temperature range. *J Am Chem Soc* 2014, **136**: 13566–13569.
[15] Tang ZY, Wang XX, He CY, *et al.* Effects of thermal expansion and four-phonon interactions on the lattice thermal conductivity of the negative thermal expansion material ScF_3. *Phys Rev B* 2024, **110**: 134320.
[16] Takenaka K, Takagi H. Giant negative thermal expansion in Ge-doped anti-perovskite manganese nitrides. *Appl Phys Lett* 2005, **87**: 261902.
[17] Yuan XL, Wang B, Sun Y, *et al.* High-entropy anti-perovskites with enhanced negative thermal expansion behavior. *Adv Funct Mater* 2024, **34**: 2404629.
[18] Wang C, Chu LH, Yao QR, *et al.* Tuning the range, magnitude, and sign of the thermal expansion in intermetallic $Mn_3(Zn,M)_x$ N(M = Ag, Ge). *Phys Rev B* 2012, **85**: 220103.
[19] Qi TF, Korneta OB, Parkin S, *et al.* Negative volume thermal expansion via orbital and magnetic orders in $Ca_2Ru_{1-x}Cr_xO_4$ ($0 < x < 0.13$). *Phys Rev Lett* 2010, **105**: 177203.
[20] Takenaka K, Okamoto Y, Shinoda T, *et al.* Colossal negative thermal expansion in reduced layered ruthenate. *Nat Commun* 2017, **8**: 14102.
[21] Hu L, Zhu YC, Fang YW, *et al.* Origin and absence of giant negative thermal expansion in reduced and oxidized Ca_2RuO_4. *Chem Mater* 2021, **33**: 7665–7674.
[22] Pan Z, Jiang XX, Yu RZ, *et al.* Transformation of thermal expansion from large volume contraction to nonlinear strong negative thermal expansion in $PbTiO_3$–$Bi(Co_{1-x}Fe_x)O_3$ perovskites. *ACS Appl Mater Inter* 2022, **14**: 23610–23616.
[23] Chen J, Xing XR, Liu GR, *et al.* Structure and negative thermal expansion in the $PbTiO_3$–$BiFeO_3$ system. *Appl Phys Lett* 2006, **89**: 101914.
[24] Pan Z, Chen J, Yu RZ, *et al.* Giant negative thermal expansion

induced by the synergistic effects of ferroelectrostriction and spin-crossover in $PbTiO_3$-based perovskites. *Chem Mater* 2019, **31**: 1296–1303

[25] Pan Z, Jiang XX, Nishikubo T, *et al.* Pronounced negative thermal expansion in lead-free $BiCoO_3$-based ferroelectrics triggered by the stabilized perovskite structure. *Chem Mater* 2019, **31**: 6187–6192.

[26] Nishikubo T, Imai T, Sakai Y, *et al.* Polar–nonpolar transition-type negative thermal expansion with 11.1% volume shrinkage by design. *Chem Mater* 2023, **35**: 870–878.

[27] Pan Z, Chen J, Jiang XX, *et al.* Enhanced tetragonality and large negative thermal expansion in a new Pb/Bi-based perovskite ferroelectric of $(1-x)PbTiO_3$–$xBi(Zn_{1/2}V_{1/2})O_3$. *Inorg Chem Front* 2019, **6**: 1990–1995.

[28] Li K, Cong S, Bian L, *et al.* Simultaneous enhancement of piezoelectricity and temperature stability in $Pb(Ni_{1/3}Nb_{2/3})O_3$–$PbZrO_3$–$PbTiO_3$ piezoelectric ceramics via Sm-modification. *J Adv Ceram* 2024, **13**: 1578–1589.

[29] Chen J, Xing XR, Yu RB, *et al.* Thermal expansion properties of lanthanum-substituted lead titanate ceramics. *J Am Ceram Soc* 2005, **88**: 1356–1358.

[30] Pan Z, Fang Y-W, Nishikubo T, *et al.* Tolerance factor control of tetragonality and negative thermal expansion in $PbTiO_3$-based ferroelectrics. *Chem Mater* 2022, **34**: 2798–2803.

[31] Kresse G, Furthmüller J. Efficient iterative schemes for *ab initio* total-energy calculations using a plane-wave basis set. *Phys Rev B Condens Matter* 1996, **54**: 11169–11186.

[32] Blöchl PE. Projector augmented-wave method. *Phys Rev B* 1994, **50**: 17953–17979.

[33] Perdew JP, Burke K, Ernzerhof M. Generalized gradient approximation made simple. *Phys Rev Lett* 1996, **77**: 3865–3868.

[34] Kohn W, Sham LJ. Self-consistent equations including exchange and correlation effects. *Phys Rev* 1965, **140**: 1133–1138.

[35] Burdett JK, McCormick TA. Electron localization in molecules and solids: The meaning of ELF. *J Phys Chem A* 1998, **102**: 6366–6372.

[36] Savin A, Nesper R, Wengert S, *et al.* ELF: The electron localization function. *Angew Chem Int Edit* 1997, **36**: 1808–1832.

[37] Dronskowski R, Bloechl PE. Crystal orbital Hamilton populations (COHP): Energy-resolved visualization of chemical bonding in solids based on density-functional calculations. *J Phys Chem-US* 1993, **97**: 8617–8624.

[38] Deringer VL, Tchougréeff AL, Dronskowski R. Crystal orbital Hamilton population (COHP) analysis as projected from plane-wave basis sets. *J Phys Chem A* 2011, **115**: 5461–5466.

[39] Maintz S, Deringer VL, Tchougréeff AL, *et al.* Analytic projection from plane-wave and PAW wavefunctions and application to chemical-bonding analysis in solids. *J Comput Chem* 2013, **34**: 2557–2567.

[40] Maintz S, Deringer VL, Tchougréeff AL, *et al.* LOBSTER: A tool to extract chemical bonding from plane-wave based DFT. *J Comput Chem* 2016, **37**: 1030–1035.

[41] Frantti J, Ivanov S, Eriksson S, *et al.* Phase Transitions of $Pb(Zr_xTi_{1-x})O_3$ Ceramics. *Phys Rev B* 2002, **66**: 064108.

[42] Burns G, Scott BA. Raman studies of underdamped soft modes in $PbTiO_3$. *Phys Rev Lett* 1970, **25**: 167–170.

[43] Burns G, Scott BA. Lattice modes in ferroelectric perovskites: $PbTiO_3$. *Phys Rev B* 1973, **7**: 3088–3101.

[44] Chen J, Xing XR, Yu RB, *et al.* Structure and enhancement of negative thermal expansion in the $PbTiO_3$–$CdTiO_3$ system. *Appl Phys Lett* 2005, **87**: 231915.

[45] Kuo SY, Li CT, Hsieh WF. Decreasing giant splitting of longitudinal and transverse optical phonons in $Pb_xSr_{1-x}TiO_3$ due to Pb covalency. *Appl Phys Lett* 2002, **81**: 3019–3021.

[46] Pan Z, Chen J, Jiang X, *et al.* Colossal volume contraction in strong polar perovskites of $Pb(Ti,V)O_3$. *J Am Chem Soc* 2017, **139**: 14865–14868.

[47] Chen J, Wang FF, Huang QZ, *et al.* Effectively control negative thermal expansion of single-phase ferroelectrics of $PbTiO_3$–$(Bi,La)FeO_3$ over a giant range. *Sci Rep-UK* 2013, **3**: 2458.

[48] Cohen RE. Origin of ferroelectricity in perovskite oxides. *Nature* 1992, **358**: 136–138.

[49] Kuroiwa Y, Aoyagi S, Sawada A, *et al.* Evidence for Pb-O covalency in tetragonal $PbTiO_3$. *Phys Rev Lett* 2001, **87**: 217601.

[50] Katsnelson MI, Naumov II, Trefilov AV. Singularities of the electronic structure and pre-martensitic anomalies of lattice properties in β-phases of metals and alloys. *Phase Transit* 1994, **49**: 143–191.[

[51] Souvatzis P, Eriksson O, Katsnelson MI. Anomalous thermal expansion in α-titanium. *Phys Rev Lett* 2007, **99**: 015901.

[52] Lohaus SH, Heine M, Guzman P, *et al.* A thermodynamic explanation of the invar effect. *Nat Phys* 2023, **19**: 1642–1648.